Nanoscale

Cite this: *Nanoscale*, 2012, **4**, 4712

www.rsc.org/nanoscale

PAPER

Large-area nanogap plasmon resonator arrays for plasmonics applications

Mingliang Jin,[a] Henk van Wolferen,[a] Herbert Wormeester,[b] Albert van den Berg[a] and Edwin T. Carlen*[a]

Received 9th March 2012, Accepted 21st May 2012
DOI: 10.1039/c2nr30576c

Large-area (~8000 mm^2) Au nanogap plasmon resonator array substrates manufactured using maskless laser interference lithography (LIL) with high uniformity are presented. The periodically spaced subwavelength nanogap arrays are formed between adjacent nanopyramid (NPy) structures with precisely defined pitch and high length density (~1 km cm^{-2}), and are ideally suited as scattering sites for surface enhanced Raman scattering (SERS), as well as refractive index sensing. The two-dimensional grid arrangement of NPy structures renders the excitation of the plasmon resonators minimally dependent on the incident polarization. The SERS average enhancement factor (AEF) has been characterized using over 30 000 individual measurements of benzenethiol (BT) chemisorbed on the Au NPy surfaces. From the 1(a_1), $\beta_{CCC} + \nu_{CS}$ ring mode (1074 cm^{-1}) of BT on surfaces with pitch λ_g = 200 nm, AEF = 0.8 × 10^6 and for surfaces with λ_g = 500 nm, AEF = 0.3 × 10^7 from over 99% of the imaged spots. Maximum AEFs > 10^8 have been measured in both cases.

Introduction

More than three decades ago the first observation of large Raman scattering enhancements from pyridine adsorbed from aqueous solution onto roughened silver electrodes was reported,[1,2] and later the enhancements were attributed to strong electromagnetic fields induced by laser excitation of localized surface plasmon resonance (LSPR) on nanoscale noble metal structures at wavelengths in the visible spectrum.[3] The large electromagnetic fields can transfer energy to molecules located near the surface of the metal nanostructures, which increases the magnitude of the induced molecular dipole, and therefore, the intensity of the inelastic scattering increases and greatly enhances the Raman scattering efficiency; this effect is called surface enhanced Raman scattering (SERS).

Currently, most SERS related research has been focused on making different shapes, sizes and arrangements of nanostructures in order to achieve a large electromagnetic enhancement factor. Almost all SERS substrates can be classified into two categories: (1) metal nanoparticles based substrates, which includes suspensions and assemblies on solid supports, and (2) nanostructures fabricated directly on solid substrates. The most common nanoparticle-based substrates are colloidal suspensions of metal nanoparticles, and various shapes and sizes have been reported.[4–10] Colloidal suspensions are attractive due to their preparation simplicity; however, they typically have poor enhancement reproducibility, which is attributed to many factors including their random composition and dimensional inhomogeneity, shape, dimer separation spacing, and excitation polarization alignment. SERS-active solid-support substrates have been reported extensively since the initial discovery of SERS. Low-cost non-lithographic methods have been reported, such as electrochemically roughened surfaces, templated surfaces,[11–14] metal island films,[15] and metal void surfaces;[16,17] however, forming small and uniform separation gaps over large surface areas remains problematic. Lithographically patterned SERS substrates remain one of the most promising methods to form large arrays of reproducible hot-spots due to the availability of advanced patterning techniques. A large variety of different nanolithography techniques are used to pattern metal nanostructures, such as electron-beam lithography, focused ion beam milling, holography, nanoimprint lithography, and laser interference lithography. Many different thin metal film nanostructures have been reported.[18–27] Surface templates fabricated by the anisotropic etching of crystalline silicon to form nanostructured surfaces with well-controlled dimensions and sharp edges have been reported, such as the commercially available inverted pyramidal pit arrays (Klarite 302, Renishaw Diagnostics, Ltd.),[28] inverted nanopyramidal pits,[29] and more recently dense arrays of subwavelength nanopyramid surfaces.[30]

Despite the impressive progress that has been made over the last three decades there is still a need for SERS substrates with large numbers of uniform scattering sites with large Raman enhancements accompanied by high reproducibility and stability. We previously reported periodic arrays of nanogap resonators arranged in two-dimensional arrays of self-aligned subwavelength nanopyramids (NPy) that were fabricated using

[a]*BIOS Lab on a Chip Group, MESA+ Institute for Nanotechnology, University of Twente, Hallenweg 15, Enschede, 7500 AE, The Netherlands. E-mail: e.t.carlen@utwente.nl; Fax: +31 53 489 3595; Tel: +31 53 489 5399*
[b]*Physics of Interfaces and Nanomaterials Group, MESA+ Institute for Nanotechnology, University of Twente, Hallenweg 15, Enschede, 7500 AE, The Netherlands. Fax: +31 53 489 3595; Tel: +31 53 489 5399*

electron beam lithography.[30] In this article, we present large area NPy substrates (entire 100 mm diameter wafer) with dense arrays of the nanogap resonators fabricated using laser interference lithography (LIL), an inexpensive and fast lithographic technique that does not require a lithography mask or reticle.[31]

Experimental

AFM imaging

Tapping mode atomic force images were recorded with a Dimension V SPM System (Veeco, USA) and ultra-sharp silicon tips with 2 nm average tip diameters (SSH, Nano-andmore, GmbH).

FDTD simulation

2D FDTD calculations were performed with Fullwave (RSoft, Inc.). Perfectly matched layer boundary conditions at the grid edges and 1 nm grid spacing were used. The complex frequency-dependent dielectric function of Au is represented by the Brendel–Borman model that is included in the simulation code. All simulations were checked for convergence.

Reflection spectroscopy

The normal incidence reflection measurement system uses a p-polarized (LPVISB100, Applied Laser Technology) white light source (100 W tungsten xenon lamp) focused on the surface with a microscope objective (10×/NA 0.3, Leica). A diaphragm is used to reduce the measurement area in the case where the surface pattern area is small. The reflected beam is collected by the same objective and passed through an analyzer (p-polarizer) through a multimode fiber (QP450-1-XSR, Ocean Optics) to the spectrometer with an integrated detector (HR4000, Ocean Optics). The certified refractive index liquids were purchased from Cargille Labs, Cedar Grove, NJ, USA; $n_d = 1.3000$ (Series AAA); $n_d = 1.5000$ (Series A); $n_d = 1.7050$ (Series M); and $n_d = 1.7200$ (Series M). The angle resolved reflectance measurements were conducted using a commercial spectroscopic ellipsometer (VASE Ellipsometer, J.A. Woollam, Inc.).

Raman measurements

The confocal Raman microscope system (alpha300R, Witech GmbH) consists of a TE-cooled charge coupled device (DU970P-BV, Andor Technology, Belfast, Northern Ireland), a He–Ne laser (150 mW; $\lambda_o = 632.8$ nm), a UHTS300 spectrometer (f/4 300 mm FL; grating: 600 lines mm^{-1}). Air measurements were imaged with 20×/0.4 NA and 100×/0.9 NA microscope objectives and water measurements from a 10^{-5} L volume of deionized water sandwiched between a glass slide and the substrate were imaged with a 100×/1.25 NA oil immersion microscope objective lens. The criteria for processing the spectra are based on determining a threshold intensity at the two vibration locations and evaluating if there is sufficient intensity that is considered a vibration mode $I_{SERS} > I_t$, where $I_t = \mu + 4\sigma$, where μ is the baseline background noise signal and σ is the standard deviation of the Gaussian distributed background noise signal. When $I_{SERS} > I_t$, then the spectra are processed and the AEF is estimated.

Results and discussion

The nanogap plasmon resonators presented in this article can couple far-field radiation into near-field electromagnetic fields in the form of LSPR. The NPy surfaces consist of a two-dimensional grid of orthogonally positioned nanogaps located at the intersection of the close-packed NPy structures. The metal nanogap plasmon resonators form standing surface waves on the opposing faces of the NPy surfaces, which couple and result in large electromagnetic fields at the base of the nanogaps.[32] Fig. 1 shows two-dimensional finite difference time domain (FDTD) numerical simulation results of the electric field distribution in the nanogap between adjacent NPy structures generated by a p-polarized plane-wave excitation.

Fig. 1a shows a two-dimensional cross-section profile of a nanogap that was measured from a typical sample using atomic force microscopy (AFM). The measured AFM profile data were imported directly into the FDTD simulator. The total electric-field magnitude $|\vec{E}_{tot}(x,z)|$ is shown in Fig. 1b and the magnitude of the magnetic field $|\vec{H}_y(x,z)|$ is shown in the inset. Fig. 1c shows high resolution scanning electron microscopy (HR-SEM) images of the metal-coated NPy surfaces with a pitch of $\lambda_g = 200$ nm. The electromagnetic field enhancement can be very large at specific locations between NPy nanostructures, called hot spots (Fig. 1b), and is defined as $g(x,z) = |\vec{E}_{tot}(x,z)|/|\vec{E}_o(x,z)|$, where $|\vec{E}_o(x,z)|$ is the electric field of the incident optical excitation with frequency ω_o. The field enhancement is an important parameter used to assess the electromagnetic SERS enhancement factor G^{EM}. The electromagnetic SERS enhancement is a consequence of the enhancement of both the incident electric field and the scattered electric field. Assuming that the enhancement is independent of the absolute photon fluxes and polarizations, the electromagnetic enhancement factor for a Stokes scattering process can be expressed as[33]

$$G^{EM}(\vec{r},\omega) = \left[\frac{E_{tot}(\vec{r},\omega_o)}{E_o(\vec{r},\omega_o)}\right]^2 \cdot \left[\frac{E_{tot}(\vec{r},\omega_o-\omega_1)}{E_o(\vec{r},\omega_o-\omega_1)}\right]^2$$

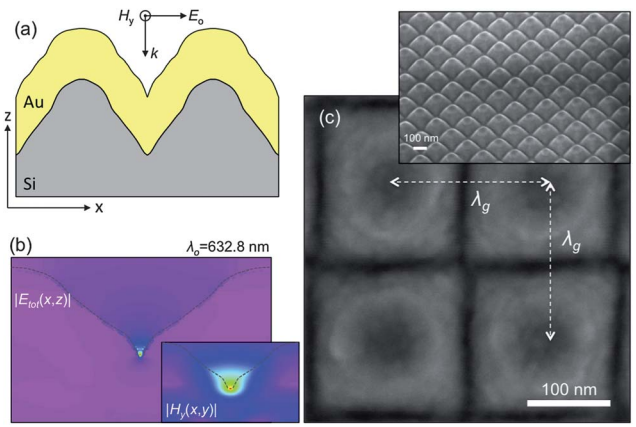

Fig. 1 Nanogap Au NPy plasmon resonators. (a) High-resolution atomic force microscopy cross-section profile converted into a two-dimensional simulation model. (b) 2D FDTD simulation results showing the spatial dependence of the total electric field $|\vec{E}_{tot}(x,z)|$ and magnetic field $|\vec{H}_y(x,z)|$ at the base of the nanogroove region. (c) HR-SEM image of a surface with $\lambda_g = 200$ nm.

where ω_o is the incident radiation frequency and the scattered radiation has vibrational frequency ω_1. The electromagnetic field enhancement results in a Raman scattering enhancement that can be approximated as $G^{EM} \approx g^4$. For the Au NPy surface modeled in Fig. 1 with a smooth Au surface, $G^{EM} \sim 10^6$.

In this article, we report large area SERS substrates patterned using LIL.[31] Fig. 2a shows the basic configuration of the LIL patterning system. The fabrication procedure is shown schematically in Fig. 2b. First, a 70 nm thick silicon nitride layer is deposited on conventional silicon (100) wafers. A negative photoresist is then spin-cast (100 nm thick) on the front side of the wafers, soft-baked (100 °C, 1 min.) and subsequently mounted on the LIL sample holder (Fig. 2a). The sample is then exposed twice in orthogonal directions and subsequently developed, thus forming an array of nanoholes in the photoresist layer (Fig. 2b). The pattern is then transferred to the silicon nitride layer by reactive ion etching (Fig. 2b). A 20 nm thick silicon dioxide layer is then reactively grown (950 °C, 20 min) on the exposed silicon regions. The silicon nitride layer was removed by immersion in phosphoric acid (180 °C, 30 min). The exposed silicon regions are then anisotropically wet etched in potassium hydroxide (50 °C, 30 s), where the 2D NPy arrays are spontaneously formed. The silicon dioxide layer is then removed in hydrofluoric acid revealing the patterned silicon surface (Fig. 2b, lower right). The final fabrication step is the deposition of the Au plasmonic layer (70 nm thick) (Fig. 2d). Fig. 2c shows a completed wafer with $\lambda_g = 200$ nm NPy arrays immersed in deionized water that shows the uniform color change on the surface due to the localized surface plasmon resonance. The inset in Fig. 2c shows how the optical reflection changes as the refractive index on the NPy Au surface is increased from $1.3000 \leq n_d \leq 1.7050$.

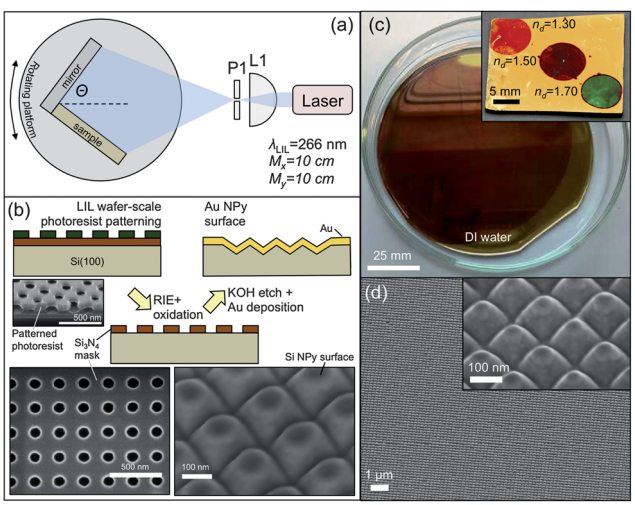

Fig. 2 Large area nanogap plasmon resonator array surfaces. (a) LIL scheme. (b) Nanofabrication process steps. (c) Patterned Au NPy surface over a 100 mm diameter silicon wafer immersed in deionized water showing the uniform reflected color change. Inset: substrate with area 1.5 × 2.0 cm^2 showing optical reflectivity with varying dielectric materials. Red region is due to a water droplet ($n_d \approx 1.33$), purple region is due to a calibrated refractive index oil with $n_d \approx 1.5$ and the green region is due to an oil with $n_d \approx 1.7$. (d) HR-SEM images of patterned Au NPy surfaces ($\lambda_g = 200$ nm).

Reflection spectroscopy is a non-destructive and non-contact technique that involves the measurement of light reflected from a nanopatterned surface, and the corresponding spectrum is recorded. However, reliable reflectance measurements are only possible when recorded from large area substrates with relatively uniform nanostructure dimensions, as is the case with the Au NPy substrates presented in this article. The reflection spectra from the Au NPy surfaces provide an indication of the wavelength (or energy) that the optical excitation generates the LSPR in the nanogaps of the NPy surfaces. Fig. 3 shows reflectance measurements from the Au NPy surfaces ($\lambda_g = 200$ nm) using four different dielectric materials. A flat (as-deposited) Au surface with the appropriate dielectric material was used as a reference for each measurement. In air ($n_d = 1.0$), the reflectance minimum wavelength occurs near 505 nm, which is very close to the first Au inter-band transition (~470 nm), and therefore, the surface plasmon resonance is weakly represented. The inset shows an image of the Au NPy surface (area: 3 cm^2) in air. A refractive index liquid with $n_d = 1.3000$ ($\Delta n_d = 0.3$) as the upper dielectric material in direct contact with the Au surface results in a clear red-shifted reflectance minimum with a wavelength of 526 nm ($\Delta\lambda \approx 21$ nm). Similarly, increasing the refractive index of the upper dielectric material with $n_d = 1.5000$ and $n_d = 1.7050$ results in a further red-shifted resonance minimum with wavelengths of 558 nm ($\Delta\lambda \approx 32$ nm) and 603 nm ($\Delta\lambda \approx 42$ nm), respectively. In each case, the inset images show the reflected color associated with the corresponding refractive index liquid, which is complementary to the color associated with the resonance wavelength from the reflectance measurements. The red-shift in resonance wavelength with increasing refractive index of the upper dielectric material is similar to Au nanospheres and shells,[34] and the 200 nm pitch Au NPy surfaces have a refractive index sensitivity ($\Delta\lambda/\Delta n_d$) of 140 nm per RIU.

Angle resolved reflectance measurements using a conventional spectroscopic ellipsometer have also been recorded. Since conventional measurement instruments use excitation sources

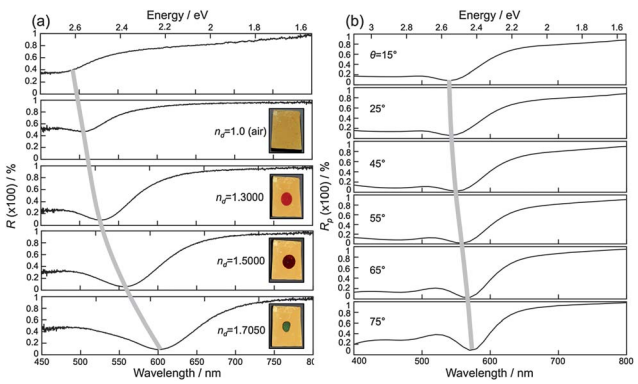

Fig. 3 Reflectance measurements of Au NPy surfaces ($\lambda_g = 200$ nm). (a) Normal incidence reflectance measurements. The reflectance from the flat Au surface is shown in the top graph. Reflection minimum red-shifts with increasing refractive index from $n_d = 1$ (air) to $n_d = 1.7050$. (b) Angle resolved p-polarized reflectance R_p measurements as a function of the incident angle θ and excitation energy. The incidence angle is varied from $15° \leq \theta \leq 75°$, where $\theta = 0°$ is normal incidence. The Au NPy surface is coated with a 100 nm-thick layer of spin cast PMMA with a refractive index $n_d \approx 1.5$.

that have large spot diameters (~1 mm), this type of measurement is only possible on highly uniform nanotextured surfaces with well controlled nanostructure dimensions over large surface areas, as in the case of the NPy surfaces patterned using LIL. Fig. 3b shows p-polarized reflectance R_p measurements from Au NPy surfaces coated with a thin layer of polymethylmethacrylate (PMMA), which has a refractive index $n_d \approx 1.5$, as a function of incidence angle θ and excitation energy. The R_p minimum at $\theta =$ 15 degrees and $n_d \approx 1.5$ corresponds well to the normal incidence reflectivity measurements (Fig. 3a, $n_d = 1.5000$). As the incidence angle is increased the reflectance minimum wavelength red-shifts, which can be attributed to a change in the momentum generated on the patterned surface as a function of incidence angle. A minimum reflectance of $R_p \approx 1\%$ occurs at an incidence angle of $\theta \approx 55$ degrees. It should be noted that reflection spectroscopy performed here uses excitation spot diameters of ~1 mm and records the average response of the respective area.

Our primary application is SERS and we have conducted an extensive study of the magnitude and uniformity of the average enhancement factor (AEF) of the Au NPy surfaces from 30 000 measurements of chemisorbed self-assembled monolayers (SAMs) of benzenethiol (BT). Benzene is a popular Raman probe molecule as it has reasonably large differential scattering cross-sections $d\sigma/d\Omega \sim 10^{-29}$ cm^2 sr^{-1},[35] is well-characterized with a relatively small number of Raman active modes, and has no optical absorption above an excitation wavelength of 400 nm. SAMs are useful for the characterization of SERS surfaces in that they allow the estimation of the molecular surface density in the measurement region. All measurements have been performed on a commercial Raman microscope system. Fig. 4 shows a representative example of the SERS spectra of a monolayer of BT chemisorbed on the Au NPy surface measured in ambient air.

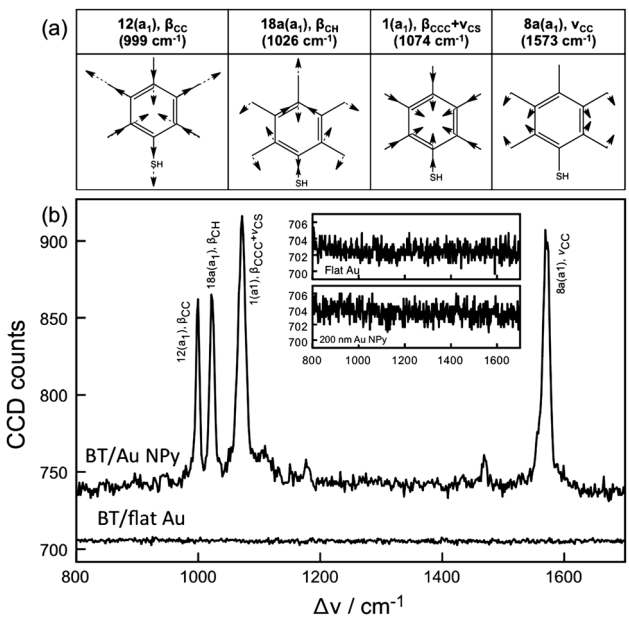

Fig. 4 Raman vibrational spectra of BT chemisorbed on Au. (a) Raman vibration mode assignments. (b) Measured SERS spectra of BT on Au NPy ($\lambda_g = 200$ nm) surface. Inset: measured Raman spectra from clean Au surfaces.

The Raman Stokes vibration modes are depicted in Fig. 4a. Each of the BT vibration modes has been previously reported.[36] The 999 cm^{-1} mode is due to the C–H waging mode. The 1026 cm^{-1} is from the C–C symmetric stretch. The 1074 cm^{-1} mode indicates the C–C asymmetric stretch and is strongly affected by the C–S bond. The last strong peak is the 1573 cm^{-1} mode, which represents the C–C symmetric stretch. Note that the 917 cm^{-1} vibration mode, associated with the S–H bending mode, that occurs for BT in free solution does not appear in the chemisorbed BT to Au and is a good indicator of the monolayer formation.[35,36] The measured spectrum of BT on a flat Au layer is also shown in Fig. 4b, and does not contain any detectable vibration peaks. The measured spectra of clean NPy and flat Au coated surfaces are shown in the inset of Fig. 4b, which show no vibrational information and establishes the background noise floor of the measurement. Additionally, a broad background signal occurs for all Au NPy measurements compared to measurements of BT on flat Au surfaces and clean Au NPy surfaces.

The SERS AEF has been characterized in terms of its magnitude and areal uniformity. Each measurement accumulates photons from a large number of BT molecules, and therefore, an AEF is used to characterize the SERS surfaces. The magnitude of the AEF has been estimated using a combination of measurements and numerical modeling to assess the electromagnetic enhancement volume of the nanogap. Only the nanogap region within the laser spot size focused with a microscope objective is considered when estimating the AEF metric. The area of enhancement region has been estimated using the 2D simulation results shown in Fig. 1c. If we assume that every molecule contributes equally to the intensity (CCD counts) of the Raman signal, then the SERS average enhancement factor can be estimated as $AEF = I_{SERS}N_{RS}(I_{RS}N_{SERS})^{-1}$, where N_{SERS} is the number of analyte molecules that contribute to the intensity of Raman signal (I_{SERS}) from the SERS substrate and N_{RS} is the number of analyte molecules that contribute to the intensity of the Raman signal (I_{RS}) without the SERS substrate. The exact number of molecules that contribute to the measured intensities is difficult to obtain; however, it can be estimated with reasonable accuracy. Since the measured I_{SERS} originates from molecules near the surface, $N_{SERS} \approx 2D_{SERS}H_{enh}L_{enh}$, where D_{SERS} is the density of the analyte molecules on the surface, $2H_{enh}$ is the height of the two surfaces in the nanogap enhancement region that contain the attached BT molecules, and L_{enh} is the length of the enhancement region, which is dependent on the laser spot size. The non-SERS Raman signal from the solution measurement depends on the characteristics of the optical collection volume and must be estimated separately to determine N_{RS}. Since conventional Raman spectroscopy is commonly done in aqueous solution, a practical approach to estimate the number of molecules is to use the concentration of the analyte. In aqueous solution, we assume everywhere that the number of molecules is the same and all the molecules in the detection volume contribute equally to I_{RS}. We define $[C_{RS}]$ as the concentration of the analyte without the SERS substrate. The number of analyte molecules in the optical detection volume can be estimated as $N_{RS} \approx [C_{RS}]A_SH_{eff}$, where A_S is the beam waist area of the excitation laser source and H_{eff} is the effective height of the optical detection volume. We use an empirical method[37] to estimate H_{eff} for

a particular measurement system configuration *i.e.* objective lens, laser source, and pin-hole. For the 20×/0.4 NA objective $H_{eff} \approx$ 14.8 μm and for the 100×/0.9 NA objective $H_{eff} \approx$ 1.9 μm. Therefore, the average enhancement factor can be estimated as

$$\mathrm{AEF} = \frac{I_{SERS} N_{RS}}{I_{RS} N_{SERS}} \approx \frac{I_{SERS}[C_{RS}] A_S H_{eff}}{2 I_{RS} D_{SERS} H_{enh} L_{enh}}$$

This modified expression is especially effective when a SAM of Raman active molecules is chemisorbed onto the Au surfaces using a thiol (–SH)–Au complex and provides a reasonably accurate estimation of the number of molecules in the measurement region.

For the SERS measurement, the number of molecules on the surface is $N_{SERS} \approx D_{SERS} H_{enh} L_{enh}$, which requires the estimation of D_{SERS}, H_{enh} and L_{enh}. The molecular surface density of the chemisorbed thiolated molecules on an Au surface is based on previous reports, $D_{SERS} \approx 5$ molecules nm^{-2}.[36] The estimation of H_{enh} and L_{enh} requires knowledge of the electromagnetic field in the nanogap, which is a function of the surface pitch, depth, geometry, metal dielectric properties, and gap dielectric medium. From Fig. 1, the profile of $|\vec{E}_{tot}(x,z)|$ as a function of distance z at the center of the nanogap $x = 0$ has been used to estimate the height of the enhancement region $H_{enh} \approx 7$ nm. It should be noted that the Au deposition method results in surfaces that are relatively rough due to grain size variations, which affects the geometry of the nanogap profile. Therefore, we expect that the electric field profile and magnitude will vary and accordingly will contribute to the overall AEF spatial variation. The length of the enhancement region L_{enh} depends on the spot size diameter of the excitation beam on the surface and the polarization alignment of the laser source to the nanogap. For all measurements the laser source polarization was aligned perpendicular to one of the directions on the NPy surface. For the 20×/0.4 NA objective $L_{enh} \approx 2$ μm and for the 100×/0.9 NA objective $L_{enh} \approx 1$ μm.

Fig. 5a–d show the Raman image maps of the four different vibrational modes (999 cm^{-1}, 1026 cm^{-1}, 1074 cm^{-1} and 1573 cm^{-1}) of BT chemisorbed on Au in an ambient air environment. Each image map contains 2500 full spectra measured over an area of 100×100 μm^2. From these Raman image maps, we can see the high spatial uniformity of the Raman measurements from the Au NPy substrate covered with a BT SAM. Measurements were performed with a 20×/0.4 NA objective lens, 5 mW laser power measured at the entrance of the microscope objective, and 100 ms integration time. Fig. 5e shows a representative SERS spectrum of a monolayer of BT on the Au NPy surface (upper spectra) and from a thin layer of neat BT solution (lower spectra). The 5000 measured spectra from the 1074 cm^{-1} and 1573 cm^{-1} modes were further processed to assess the spatial distribution of the AEF. The 2500 spectra of each vibration mode were filtered by choosing only the spectra that contained a detectable peak at the known vibration frequency.

Fig. 6 shows histograms of the estimated AEF for the two vibration modes. Both histograms can be modeled as a log-normal distribution. For the 1074 cm^{-1} mode, 80% of the measurement locations contained measurable spectra with a mean AEF = 0.6 × 10^6 and maximum AEF = 0.8 × 10^7. The standard lower deviation with 95% confidence interval is 0.4 × 10^6 and the standard upper deviation is 0.8 × 10^6. The spectra of the 1573 cm^{-1} vibration mode were detected at 60% of the measurement locations with a mean AEF = 0.5 × 10^6 and maximum AEF = 0.4 × 10^7. The standard lower deviation with 95% confidence interval is 0.3 × 10^6 and the standard upper deviation is 0.8 × 10^6. For these measurements we did not detect any damage to the BT monolayer during imaging.

Similar measurements were done in an ambient air environment using a 100×/0.9 NA microscope objective, which reduces the excitation laser spot and subsequently the number of molecules measured for each of the 2500 measurements. Fig. 7a shows a representative Raman spectrum from the BT monolayer chemisorbed to the Au NPy surface (upper spectra) and a small volume neat solution of BT (lower spectra). Fig. 7b shows the AEF distribution of 1950 measured spectra of the 1074 cm^{-1} vibration mode imaged over an area of 40 × 40 μm^2. The AEF distribution also follows a log-normal distribution with mean AEF = 0.08 × 10^7 and maximum AEF > 10^8 and about 80% of the imaged spots contained measurable spectra. The standard lower deviation with 95% confidence interval is 0.06 × 10^7 and the standard upper deviation is 0.2 × 10^7.

Fig. 8a shows normal incidence reflectance measurements from a Au NPy surface with pitch λ_g = 500 nm, where the local surface plasmon resonance is more closely aligned to the 632.8 nm He–Ne laser wavelength and a larger AEF is expected. A total of 5000 Raman measurements of BT SAM on Au NPy surfaces with pitch λ_g = 500 nm over an area of 40 × 40 μm^2 in

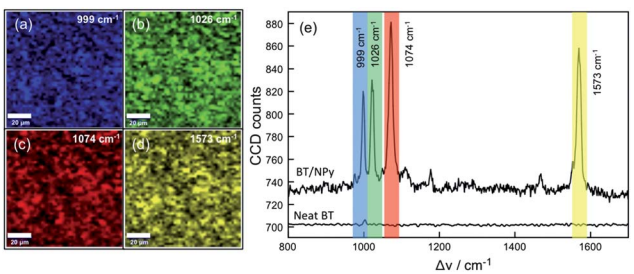

Fig. 5 Raman measurements of BT on the Au NPy surface (λ_g = 200 nm) measured in air using a 20×/0.4 NA objective, 5 mW laser power measured at the entrance of the objective, and 100 ms integration time. (a)–(d) Spatial Raman maps over an area of 100 × 100 μm^2 of the different BT vibration modes (999 cm^{-1}, 1026 cm^{-1}, 1074 cm^{-1} and 1573 cm^{-1}). (e) Representative SERS spectra of BT on the Au NPy surface (upper) and non-SERS Raman spectra from a small volume neat BT solution.

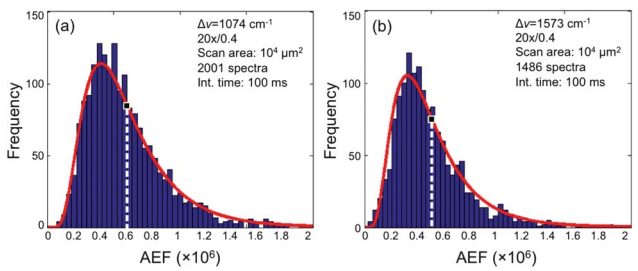

Fig. 6 Histograms of the AEF distribution from selected spectra of 2500 measurements over the imaged area (100 × 100 μm^2) in air from Au NPy surfaces (λ_g = 200 nm; white dashed lines represent distribution mean). (a) Raman vibration mode 1074 cm^{-1} distribution of 2001 measurements. (b) Raman vibration mode 1573 cm^{-1} distribution of 1486 measurements.

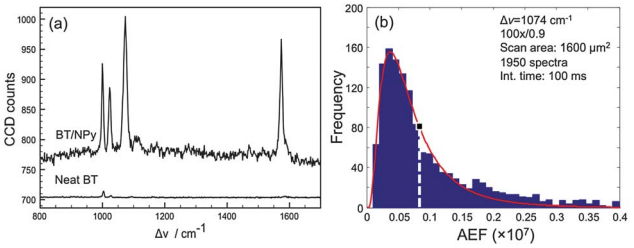

Fig. 7 Raman vibrational measurements of BT. (a) Representative SERS measurement of BT in air on the Au NPy surface (λ_g = 200 nm; white dashed lines represent distribution mean) using 100×/0.9 NA objective imaged over a 40 × 40 μm² area and a Raman measurement of neat BT. (b) Histogram of the AEF distribution from 1950 spectra over the imaged area.

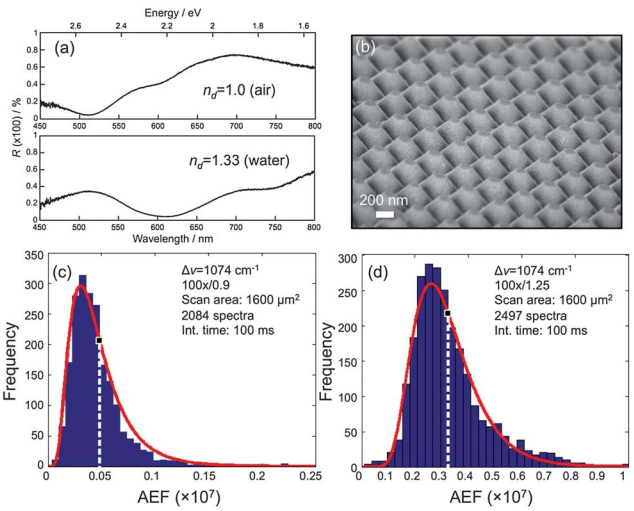

Fig. 8 Measurements from a Au NPy surface with pitch λ_g = 500 nm (white dashed lines represent distribution mean). (a) Normal incidence reflectance measurements normalized to a non-patterned Au surface. Reflection minimum red-shifts with increasing refractive index from n_d = 1(air) to n_d = 1.33 (water). (b) HR-SEM image. (c) and (d) Histograms of the AEF distribution of the 1074 cm^{-1} mode from selected spectra of 2500 measurements over the imaged area (40 × 40 μm²). (c) AEF distribution of 2084 measurements in air using 100×/0.9 NA objective. (d) AEF distribution of 2497 measurements in water using 100×/1.25 NA oil immersion objective.

both air and water have been recorded. Fig. 8c and d show the AEF histograms of the measured spectra of the 1074 cm^{-1} vibration mode (for each measurement) over the imaged area in air (Fig. 8c) and in water (Fig. 8d). Both AEF histograms can be accurately modeled with a log-normal probability distribution function. The air measurements contained measurable spectra from 83% of the measurement locations with mean AEF = 0.5 × 10^6 and maximum AEF ≈ 10^6. The standard lower deviation with 95% confidence interval is 0.3 × 10^6 and the standard upper deviation is 0.7 × 10^6. The water measurements contained measurable spectra from 99.88% of the measured locations with mean AEF = 0.3 × 10^7 and maximum AEF > 10^8. The standard lower deviation with 95% confidence interval is 0.2 × 10^7 and the standard upper deviation is 0.4 × 10^7. From the presented AEF spatial distributions we see that the standard deviation range (95% confidence interval) is rather large. We attribute this large range to the rough Au surface and non-uniform surface coverage of the BT molecules. The rough surface creates a variation of the nanogap dimensions, which results in measured enhancements much larger than the calculated enhancement and the large upper range of the log-normal distribution. Controlling the deposition conditions, flame annealing, or chemical polishing can reduce the Au surface roughness. The non-uniform BT coverage should result in reduced Raman intensities as the number of molecules is reduced. Previous reports indicate similar large AEF standard deviations.[27,35] In addition to the sample AEF spatial distribution, we have compiled a small dataset of sample-to-sample variations and report repeatability in the 90–95% range provided that the BT formation and surface coverage are similar.

The Au NPy (λ_g = 500 nm) surfaces are compared to commercially available inverted pyramidal pit array SERS substrates (Klarite 302, Renishaw Diagnostics, Ltd). A BT monolayer was chemisorbed onto each substrate surface using the previously described preparation method. Fig. 9a–d show measurement results from the Klarite 302 substrates with chemisorbed BT. The Klarite 302 substrate (Fig. 9d) with chemisorbed BT was measured in air using a 2 mW power measured at the entrance of the microscope objective. A 100×/0.9 NA objective was used to record 10 000 spectra over an area of 40 × 40 μm² (Fig. 9b). A representative BT spectrum from the Klarite substrates is shown in Fig. 9a. The Raman image map shown in Fig. 9b represents the measured CCD

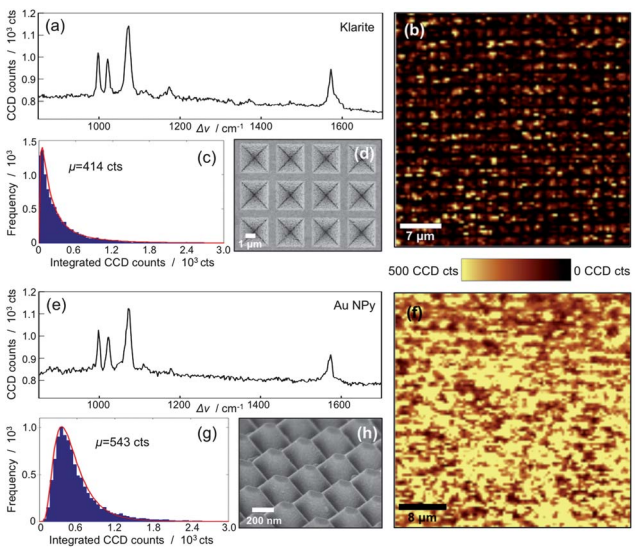

Fig. 9 Comparison of Au NPy and Klarite 302 SERS substrates using 20 000 measurements of the 1074 cm^{-1} vibrational mode of chemisorbed BT over areas of 40 × 40 μm² using a 2 mW power measured at the entrance of the microscope objective and 100 ms integration time. (a)–(d) Klarite 302 SERS substrate measurements in air using 100×/0.9 NA objective. (a) Representative SERS spectrum. (b) Spatial map from 10 000 measurements. (c) Histogram of the integrated CCD counts. (d) HR-SEM image of the SERS surface. (e)–(h) Au NPy (λ_g = 500 nm) substrate measurements in water using 100×/1.25 NA oil immersion objective. (e) Representative SERS spectrum. (f) Spatial map from 10 000 measurements. (g) Histogram of the integrated CCD counts. (h) HR-SEM image of the SERS Au NPy surface.

counts over the spectral range from 1060 cm^{-1} to 1090 cm^{-1}. Fig. 9c shows a histogram of the integrated CCD count distribution. Fig. 9e–h show the measured results from the Au NPy substrates with chemisorbed BT. The Au NPy substrates (Fig. 9h) with chemisorbed BT were measured in water using the same measurement configuration with a 100×/1.25 NA oil immersion microscope objective to record 10 000 spectra over an area of 40 × 40 μm^2. A representative BT spectrum from the Au NPy substrates is shown in Fig. 9e. The image shown in Fig. 9f represents the measured CCD counts over the spectral range from 1060 cm^{-1} to 1090 cm^{-1}. Fig. 9g shows a histogram of the integrated CCD count distribution. From the measurements shown in Fig. 9, the histogram of the CCD counts recorded from Klarite 302 substrate follows a log-normal distribution with a mean measurement of 414 CCD counts. The histogram of the CCD counts recorded from Au NPy substrates has a mean measurement of 543 CCD counts. The Au NPy substrates have a similar mean CCD count and much smaller variance for the measurement conditions presented here. The most striking difference between the two substrates is that the Au NPy substrates provide measurable spectra from 99.95% of the measured locations compared to 53.58% from the Klarite 302 substrates. The comparison with the Klarite substrate highlights the importance of having a spatial density of hot-spot scattering sites. The Klarite substrates have a significant amount of surface area that does not produce a measurable signal, which is evident in the large number of CCD counts near zero in the histogram shown in Fig. 9c. The Au NPy surfaces produce measureable signals in nearly every measurement site as shown in the histogram in Fig. 9g.

Conclusions

Large area metal nanogap plasmon resonator array substrates manufactured using laser interference lithography have been presented. The new substrates have a large nanogap density; a surface area of 4 cm^2 contains about 4 km length of nanogaps. The large area SERS substrates have been characterized with over 30 000 measurements of chemisorbed BT molecules and a log-normal distribution model was found to describe the areal distribution statistics of the AEF. The extracted mean areal AEF from the SERS surfaces with pitch $\lambda_g = 200$ nm is AEF = 0.8×10^6 and for surfaces with $\lambda_g = 500$ nm the mean AEF = 0.3×10^7. Maximum AEF > 10^8 have been measured in both cases. The new large area SERS substrates are suitable for both basic research and commercial applications.

Acknowledgements

The authors thank Mark Smithers for making all of the HR-SEM images.

Notes and references

1 M. Fleischmann, P. J. Hendra and A. J. McQuillan, *Chem. Phys. Lett.*, 1974, **26**, 163.
2 D. L. Jeanmaire and R. P. VanDuyne, *J. Electroanal. Chem.*, 1977, **84**, 1.
3 M. Moskovits, *J. Chem. Phys.*, 1978, **69**, 4159.
4 M. Moskovits, *J. Raman Spectrosc.*, 2005, **36**, 485.
5 S. Link and M. A. El-Sayed, *J. Phys. Chem. B*, 1999, **103**, 8410.
6 H. Wang, D. W. Brandl, F. Le, P. Nordlander and N. J. Halas, *Nano Lett.*, 2006, **6**, 827.
7 Y. Lu, G. L. Liu, J. Kim, Y. X. Mejia and L. P. Lee, *Nano Lett.*, 2005, **5**, 119.
8 J. M. McLellan, Z. Y. Li, A. R. Siekkinen and Y. N. Xia, *Nano Lett.*, 2007, **7**, 1013.
9 L. Rodríguez-Lorenzo, R. A. Álvarez-Puebla, I. Pastoriza-Santos, S. Mazzucco, O. Stéphan, M. Kociak, L. M. Liz-Marzán and F. J. García de Abajo, *J. Am. Chem. Soc.*, 2009, **131**, 4616.
10 J. B. Jackson and N. J. Halas, *Proc. Natl. Acad. Sci. U. S. A.*, 2004, **101**, 17930.
11 S. Coyle, C. M. Netti, J. J. Baumberg, M. A. Ghanem, P. R. Birkin, P. N. Bartlett and D. M. Whittaker, *Phys. Rev. Lett.*, 2001, **87**, 176801.
12 S. Shanmukh, L. Jones, J. Driskell, Y. Zhao, R. Dluhy and R. A. Tripp, *Nano Lett.*, 2006, **6**, 2630.
13 H. Masuda and K. Fukuda, *Science*, 1995, **268**, 1466.
14 D. Choi, Y. Choi, S. Hong, T. Kang and L. P. Lee, *Small*, 2010, **6**, 1741.
15 J. C. Hulteen and R. P. Van Duyne, *J. Vac. Sci. Technol., A*, 1995, **13**, 1553.
16 L. Y. Wu, B. M. Ross and L. P. Lee, *Nano Lett.*, 2009, **9**, 1956.
17 P. N. Bartlett, P. R. Birkin and M. A. Ghanem, *J. Chem. Soc., Chem. Commun.*, 2000, **17**, 1671.
18 S. C. Kitson, W. L. Barnes and J. R. Sambles, *Phys. Rev. Lett.*, 1996, **77**, 2670.
19 L. Gunnarsson, E. J. Bjerneld, H. Xu, S. Petronis, B. Kasemo and M. Käll, *Appl. Phys. Lett.*, 2001, **78**, 802.
20 Z. Li, W. M. Tong, W. F. Stickle, D. L. Neiman and R. S. Williams, *Langmuir*, 2007, **23**, 5135.
21 N. A. Abu Hatab, J. M. Oran and M. J. Sepaniak, *ACS Nano*, 2008, **2**, 377.
22 A. G. Brolo, E. Arctander, R. Gordon, B. Leathem and K. L. Kavanagh, *Nano Lett.*, 2004, **4**, 2015.
23 D. P. Fromm, A. Sundaramurthy, P. J. Schuck, G. Kino and W. E. Moerner, *Nano Lett.*, 2004, **4**, 957.
24 J. A. Porto, F. J. Garcia-Vidal and J. B. Pendry, *Phys. Rev. Lett.*, 1999, **83**, 2845.
25 D. Xuegong, G. B. Braun, S. Liu, P. F. Sciortino, Jr, B. Koefer, T. Tombler and M. Moskovits, *Nano Lett.*, 2010, **10**, 1780.
26 P. Mandall and S. A. Ramakrishna, *Opt. Lett.*, 2011, **36**, 3705.
27 M. R. Gartia, Z. Xu, E. Behymer, H. Nguyen, J. A. Britten, C. Larson, R. Miles, M. Bora, A. S.-P. Chang, T. C. Bond and G. L. Liu, *Nanotechnology*, 2010, **21**, 395701.
28 N. M. B. Perney, J. J. Baumberg, M. E. Zoorob, M. D. B. Charlton, S. Mahnkopf and C. M. Netti, *Opt. Express*, 2006, **14**, 847.
29 H. Gao, J. Henzie, M. H. Lee and T. W. Odom, *Proc. Natl. Acad. Sci. U. S. A.*, 2008, **105**, 20146.
30 M. L. Jin, V. Pully, C. Otto, A. van den Berg and E. T. Carlen, *J. Phys. Chem. C*, 2010, **114**, 21953.
31 H. van Wolferen and L. Abelmann, Laser interference lithography, in *Lithography: Principles, Processes and Materials*, ed. T. C. Hennessey, Nova Science Publishers, Inc., 2011.
32 M. B. Sobnack, W. C. Tan, N. P. Wanstall, T. W. Preist and J. R. Sambles, *Phys. Rev. Lett.*, 1998, **80**, 5667.
33 A. Otto, Surface-enhanced Raman scattering: "classical" and "chemical" origins, in light scattering in solids IV, in , *Topics in Applied Physics*, ed. M. Cardona and G. Güntherodt, Springer-Verlag, 1984.
34 Y. Sun and Y. Xia, *Anal. Chem.*, 2002, **74**, 5297.
35 R. L. Aggarwal, L. W. Farrar, E. D. Diebold and D. L. Polla, *J. Raman Spectrosc.*, 2009, **40**, 1331.
36 J. D. Caldwell, O. Glembocki, F. J. Bezares, N. D. Bassim, R. W. Rendell, M. Feygelson, M. Ukaegbu, R. Kasica, L. Shirey and C. Hosten, *ACS Nano*, 2011, **5**, 4046.
37 B. Ren, X. F. Lin, Y. X. Jiang, P. G. Cao, Y. Xie, Q. J. Huang and Z. Q. Tian, *Appl. Spectrosc.*, 2003, **57**, 419.

